

## Isostructural phase transition-induced piezoelectricity in all-inorganic perovskite $\text{CsPbBr}_3$ for catalytic $\text{CO}_2$ reduction

Jie He<sup>a</sup>, Xuandong Wang<sup>b</sup>, Pengju Feng<sup>a,\*</sup>, Yingtang Zhou<sup>c,\*</sup>, Kai Wang<sup>d</sup>, Bo Zou<sup>d,\*</sup>, Mingshan Zhu<sup>a,\*</sup>

<sup>a</sup> College of Chemistry and Materials Science, School of Environment, Jinan University, Guangzhou 511443, PR China

<sup>b</sup> School of Environment and Chemical Engineering, Foshan University, Foshan 528000, PR China

<sup>c</sup> Zhejiang Key Laboratory of Petrochemical Environmental Pollution Control, National Engineering Research Center for Marine Aquaculture, Marine Science and Technology College, Zhejiang Ocean University, Zhoushan 316004, PR China

<sup>d</sup> State Key Laboratory of Superhard Materials, College of Materials Science and Engineering, Jilin University, Changchun 130012, PR China



### ARTICLE INFO

#### Keywords:

Isostructural phase transition  
All-inorganic perovskite  
 $\text{CsPbBr}_3$   
Piezo-catalysis  
 $\text{CO}_2$  reduction

### ABSTRACT

One charming characteristic of all-inorganic halide perovskites is their phase transition behavior which always generates an asymmetry-induced piezoelectric property under external stimuli. Here, under vibration pressure, an isostructural phase transition (IPT)-induced piezoelectricity occurs in a nanocube-like  $\text{CsPbBr}_3$  (CPB NC) to achieve catalytic reduction of  $\text{CO}_2$ . Yields of reduction products reach to  $7 \mu\text{mol g}^{-1} \text{h}^{-1}$  ( $\text{CH}_4$ ) and  $16 \mu\text{mol g}^{-1} \text{h}^{-1}$  ( $\text{CO}$ ), respectively, which are higher yet more stable than that of conventional photocatalytic  $\text{CO}_2$  reduction by CPB NC and other state-of-the-art halide perovskites. Theoretical calculations and exhaustive characterizations including *in-situ* high-pressure tests and atomic force microscopy confirm CPB NC carries out the IPT process to form polarized electric-field with high-piezoelectric potential which drives band tilting to excite piezoelectric carriers in  $\text{CO}_2$  reduction. This study reveals phase transition engineering with piezoelectric effect and marks a new step towards  $\text{CO}_2$  conversion with halide perovskites.

### 1. Introduction

Over the past few years, structural-phase transition engineering has become an emerging strategy to acquire the optimum reactive catalysts in heterogeneous catalysis [1,2]. The most important basic principle of phase transition engineering is to regulate the crystal structures and electron states of materials, which enables the improvement of catalytic activity [3,4]. One of the classic applications of phase transition strategy is to achieve the phase transformation between 2H (trigonal prismatic) and 1T (octahedral) phases in transition metal dichalcogenides (TMDs), endowing them with high catalytic activity towards various redox reaction [5,6]. Besides of these bulk phase transition in TMDs, another common phase transition type *viz.* isostructural phase transition (IPT) always happens in the perovskite materials under external stimuli such as pressure [7–12]. For example,  $\text{CsPbBr}_3$  (CPB) perovskite can go through an isostructural solid–solid phase transition which turns an ambient orthorhombic phase ( $\gamma$ -phase) into a second orthorhombic phase under pressure and this IPT primarily changes the symmetry of cations and anions to obtain the desired physiochemical property [13].

Besides, when these  $\text{CsPbBr}_3$  perovskite materials upon external stimuli,  $\text{Pb–Br}$  bond lengths and  $\text{Pb–Br–Pb}$  bond angles will shrinkage or stretch simultaneously. These changes of bond lengths and angles bring a distorted asymmetric structure, which will cause a polar and noncentrosymmetric structure with piezoelectric property [14,15]. For example, Yuan et al. gave the evidences for piezoelectricity of CPB quantum dots (QDs), that is attributed to the distortion of octahedral  $[\text{PbBr}_6]^{4-}$  and off-center Cs ion with temperature variation [16]. Such a piezoelectricity enables CPB to trigger a piezo-phototronic effect. Wang's group proved that this piezo-phototronic effect of CPB QDs succeeded to tune a spin–orbit coupled photoluminescence, showing a promising optoelectronic applications [17]. In addition to piezo-phototronic field, the piezoelectricity has recently become a new yet star catalytic technology in various redox reactions [18–27]. A well-known instance is that Ito et al. have reported a ball milling piezoelectric-process using  $\text{BaTiO}_3$  for redox-activation, opening a new avenue for the direct utilization of piezoelectric polarization charges in redox reaction [28]. Moreover, Gao's group prepared a piezoelectric membrane to transform pressure pulses into electroactive responses for foulant degradation, through

\* Corresponding authors.

E-mail addresses: [pfeng@jnu.edu.cn](mailto:pfeng@jnu.edu.cn) (P. Feng), [zhouyingtang@zjou.edu.cn](mailto:zhouyingtang@zjou.edu.cn) (Y. Zhou), [zoubo@jlu.edu.cn](mailto:zoubo@jlu.edu.cn) (B. Zou), [zhumingshan@jnu.edu.cn](mailto:zhumingshan@jnu.edu.cn) (M. Zhu).

reactive oxygen species production [29]. Nevertheless, applications in piezoelectric catalysis by exploring the intrinsic sources of piezoelectricity of piezoelectric materials (such as phase transition) are rarely reported.

Enlightened by these,  $\text{CsPbBr}_3$  nanocubes (CPB NC) were prepared herein, and showed the piezoelectric polarization caused by asymmetry breaking in an IPT process under mechanical vibration, which was the first time applied for catalytic  $\text{CO}_2$  reduction. The as-prepared CPB NC exhibited a preferable piezo-catalytic  $\text{CO}_2$  reduction activity to produce  $\text{CH}_4$  and CO with yields of 7 and  $16 \mu\text{mol g}^{-1} \text{h}^{-1}$  that are 1.5 and 2 times as high as the yield of solar light-driven catalytic activity, respectively. *In-situ* pressure-dependent Raman along with photoluminescence spectra, and a piezo-response force microscope technology all elucidated that the IPT brought about an asymmetry breaking of CPB NC to induce piezoelectricity. Systematic experiments and theory calculations further revealed that the piezoelectric polarized field produced high piezoelectric potential, changing the band structure of CPB NC to provide piezoelectric electrons towards  $\text{CO}_2$  conversion.

## 2. Experimental section

### 2.1. Synthesis of $\text{CsPbBr}_3$ nanocube

The  $\text{CsPbBr}_3$  nanocube (CPB NC) were synthesized *via* a simple method of one-pot ultrasonication (Fig. S1). Typically,  $\text{Cs}_2\text{CO}_3$  of 0.1 mmol and  $\text{PbBr}_2$  of 0.3 mmol worked as precursor powders and were added into the mixed solvent of 10 mL octadecene with 0.5 mL oleic acid and 0.5 mL oleylamine as organic ligands. The mixture was followed by tip-sonication using an ultrasonic homogenizer (JY92-IIIDN, China) with a single probe at a certain power within different time. The power and time of ultrasonication determine the morphologies of CPB. CPB NC was grown under 175 W power (50 % of the total power) for 90 min, while the applying frequency of the amplitude transformer was 20 kHz. The ultrasonication was kept a process of 3 s on and 3 s off. During the ultrasonic reaction, the colorless reaction medium gradually transformed into a faint yellow and then a bright yellow solution, which showed a green fluorescence under a 365 nm UV light excitation (Fig. S2). After reaction, the mixture were collected *via* centrifugation and washing by n-hexane. In the end, the product was collected by drying at 40 °C under vacuum condition for 12 h.

### 2.2. Piezoelectric catalytic $\text{CO}_2$ reduction

$\text{CO}_2$  reduction experiments were performed in a 60 mL sealed Pyrex bottle. Briefly, 5 mg piezoelectric catalyst, 5 mL ethyl acetate with  $50 \mu\text{L}$   $\text{Na}_2\text{SO}_3$  aqueous solution (0.025 M) were added into the bottle. The tiny amount of  $\text{Na}_2\text{SO}_3$  aqueous solution could act as a electron donor and provide  $\text{H}^+$  generation of  $\text{H}_2$  and  $\text{CH}_4$  without damaging the crystal structure of CPB. After pumping  $\text{N}_2$  (99.999 %) into the bottle to exhaust air for 20 min,  $\text{CO}_2$  (99.999 %) would be injected in the sealed bottle until the whole mixture system was filled with  $\text{CO}_2$  (0.05 MPa). The pressure used in piezoelectric catalysis was provided by a ultrasonic vibration cleaner (KS-100DE, Kunshan) that had 40 kHz frequency and 120 W maximum power. In order to aviod temperature affected by ultrasonic cavitation, circulating water would be introduced into the ultrasonic cleaner to keep the temperature of reactor at  $25 \pm 1$  °C. A gas chromatograph (GC-2014c, SHIMADZU, Japan) was used to detect the products in  $\text{CO}_2$  reduction system. The scheme of whole reaction system is shown as Fig. S3.

### 2.3. *In-situ* characterizations under high pressure

The *in-situ* Raman was tested by a high-pressure spectrometer equipped with a liquid nitrogen CCD (iHR 550, Symphony II, Horiba Jobin Yvon) under excitation of a 785 nm single-mode DPSS laser. An optical fiber spectrometer (Ocean Optics, QE65000) with a 355 nm line

of a UV DPSS laser was utilized to carry out *in-situ* PL tests. A camera (Canon Eos 5D mark II) equipped on a microscope was used to get the micrographs of the sample. *In-situ* UV-vis absorption spectra under high pressure were measured with using a deuterium halogen light source.

## 3. Results and discussion

### 3.1. Characterizations and isostructural phase transition (IPT) in CPB NC

CPB NC was synthesized through a one-pot ultrasonication, and element mapping (Fig. S4) reveals the successful synthesis of CPB NC. The CPB NC was then carried out to catalytic  $\text{CO}_2$  reduction under ultrasonic vibration in the absence of light irradiation. Fig. 1a presents a stable upward trend of two kinds of reduction products during the  $\text{CO}_2$  conversion using CPB NC, and reaches the yield of  $\text{CH}_4$  and CO at  $21 \mu\text{mol g}^{-1}$  and  $48 \mu\text{mol g}^{-1}$  within 3 h, respectively, which is much higher than that using traditional piezoelectric  $\text{BaTiO}_3$  (BTO) ( $\text{CH}_4$  of  $2 \mu\text{mol g}^{-1}$  and CO of  $5 \mu\text{mol g}^{-1}$ ). The crystal phase of the fresh and used CPB NC were investigated by XRD. As shown in Fig. 1b, typical peaks at 15.2, 21.5, 26.5, 30.6, 34.4, 37.8 and 43.9° were observed for fresh CPB NC, which were assigned to planes of orthorhombic phase (phase I) with  $Pbnm$  space group ( $a = 8.37 \text{ \AA}$ ,  $b = 8.46 \text{ \AA}$ ,  $c = 12.02 \text{ \AA}$ ) [30]. After ultrasonic treatment, all above diffraction peaks had a slight shift to higher angles. Note that opposite peak intensity of (002) and (200) peaks for fresh and used samples were observed, which revealed changes of lattice constant and exposed crystal planes [31], resulting in a new orthorhombic phase II ( $a = 8.36 \text{ \AA}$ ,  $b = 8.47 \text{ \AA}$ ,  $c = 12.29 \text{ \AA}$ ). Such phase II manifests an isostructural transition of orthorhombic phase over CPB NC after ultrasonic treatment. The simulated XRD of CPB NC through VESTA (Fig. S5) under different pressures was investigated and showed the change of unit cell parameters for space groups.

On the basic of transmission electron microscopy (TEM) pictures (Fig. 1c and d), CPB NC arranges closely as a cube-like morphology with sizes of 50–150 nm, and the lattice fringe of  $5.82 \text{ \AA}$  is accordant with d-spacing of (100) crystal plane (Fig. 1e) [30]. After ultrasonic treatment, CPB NC still maintained the cube shape (Fig. 1f and g). Notably, the lattice fringe of CPB NC changed after reaction from high resolution TEM (HRTEM) (Fig. 1h), indicating a crisscross of (001) plane of  $5.87 \text{ \AA}$  d-spacing and (100) plane of  $5.82 \text{ \AA}$  d-spacing, which was matched well with the result of opposite intensity of (002) and (200) peaks in XRD. It can be observed that there is a slight passivation at the edges and corners of CPB NC after a long-term ultrasonic vibration. This is likely due to the constant collision among the nanocubes under the effect of pressure provided by the ultrasound process, which leads to the slight blurring of TEM imaging. Fortunately, this does not affect the stability of morphological structure over CPB NC. The electron diffraction patterns (Fig. S6) of the fresh CPB NC possesses a direction along with [001] orientation which shows the orthorhombic phase in CPB structure [8]. After applying ultrasonic vibration, the crystal structure of CPB grew along [110] direction. Such an exposure of asymmetrical crystal planes suggests the isostructural transition of orthorhombic phase in CPB NC. By comparison, there is no significant change in the XRD and TEM of BTO before and after reaction (Fig. S7), thereby occurrence of the IPT is proposed to induce the efficient  $\text{CO}_2$  reduction *via* CPB NC.

### 3.2. IPT-induced piezoelectricity in CPB NC

It is known that when halide perovskites are under an external force, bond lengths and angles will change to induce a distorted asymmetric structure. This breaking of symmetry will generate a polar and non-centrosymmetric structure with a piezoelectric property. Accordingly, when an IPT of orthorhombic phase I to orthorhombic phase II over CPB NC occurs, a structural change called asymmetry breaking also happens and induces the piezoelectric polarization in CPB NC (Fig. 2). The in-depth understandings of this phenomenon are investigated by following characterizations.

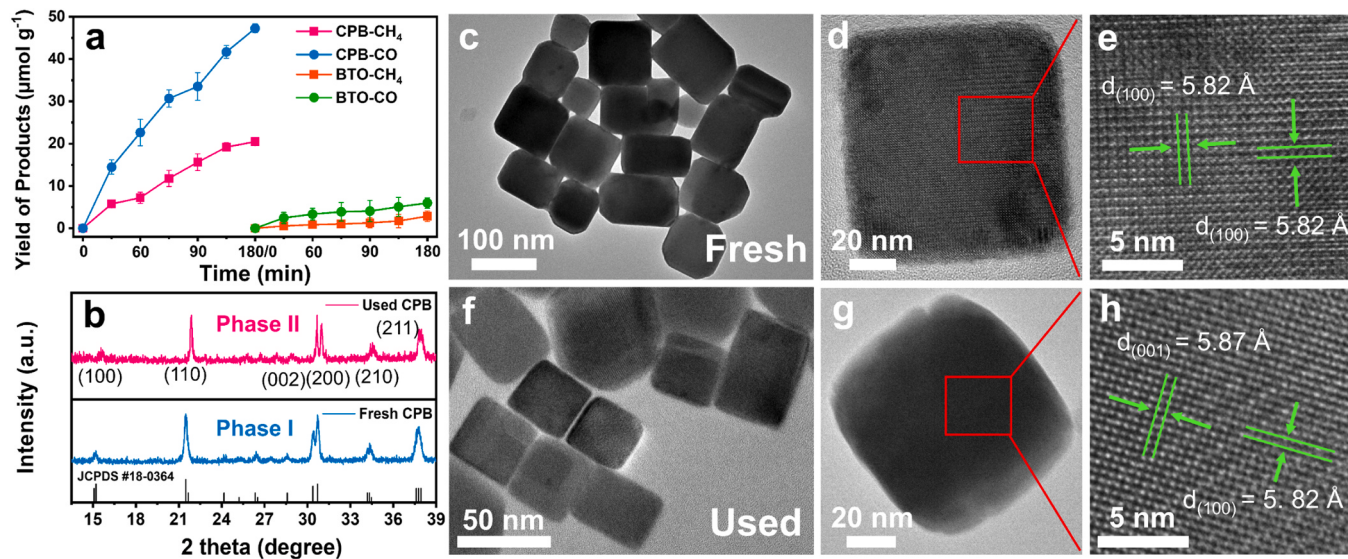


**Fig. 1.** (a) Yields of products using CPB NC and BTO in catalytic CO<sub>2</sub> reduction under ultrasonic vibration. (b) XRD patterns of used and fresh CPB NC. TEM, enlarged TEM and HRTEM images of (c)-(e) fresh and (f)-(h) used CPB NC.

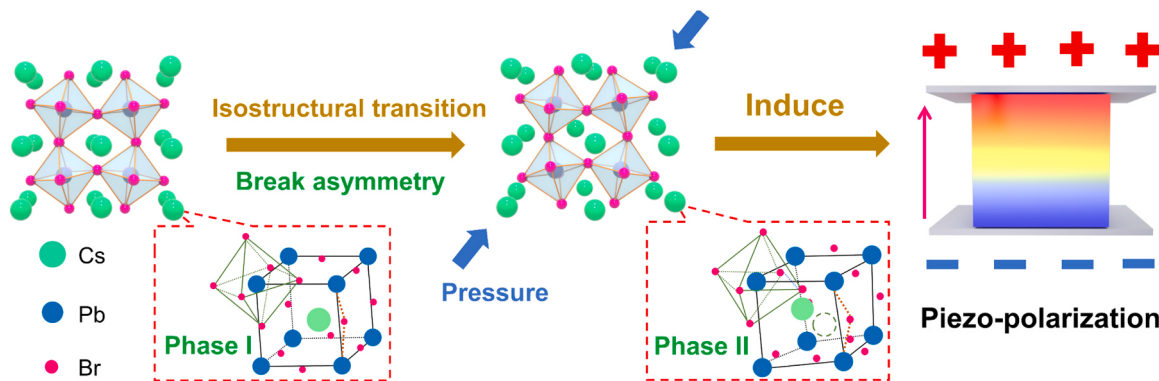


**Fig. 2.** Schematic diagram of IPT-induced piezoelectric polarization in CPB NC.

Firstly, *in-situ* Raman spectra of as-synthesized CPB NC under different pressure are depicted in Fig. 3a. It exhibits three Raman-active modes at 67.7, 86.4 and 132.2 cm<sup>-1</sup> at an ambient condition (0 GPa). The peaks at 67.7 and 86.4 cm<sup>-1</sup> named  $\nu_1$  and  $\nu_2$  modes belong to vibrational modes of Pb-Br network and [PbBr<sub>6</sub>]<sup>4-</sup> octahedron, respectively, and the other weak signal at 132.2 cm<sup>-1</sup> ( $\nu_3$  mode) is related to motion of Cs<sup>+</sup> cations [9,32]. With enhancing pressure, signals of  $\nu_1$  and  $\nu_2$  modes generate blue shift to reveal Pb-Br bonds shrinking. The intensity of  $\nu_2$  mode signal decreases with improving pressure, implying that a variation appears in Pb-Br network structures due to an anabatic distortion of [PbBr<sub>6</sub>]<sup>4-</sup> octahedron [31]. When applying pressure enhances to 2.0 GPa, the  $\nu_3$  mode of Cs<sup>+</sup> still exists. This means that structural connection between Cs<sup>+</sup> and Pb-Br network structure has not been destroyed by the intense distortion and compression of octahedron cavity. On one hand,  $\nu_3$  mode also shifts to a higher wavenumber under higher pressure, demonstrating that the center Cs<sup>+</sup> of CPB NC gradually shifts with pressure applied. On the other hand, the  $\nu_2$  mode generates splitting signals under 2.0 GPa pressure owing to a phase transition of orthorhombic [PbBr<sub>6</sub>]<sup>4-</sup> octahedron.

*In-situ* pressure-induced photoluminescence (PL) spectra profoundly reveal the effect of pressure for phase transition of CPB NC (Fig. 3b-c). Under ambient condition, CPB NC shows an apparent PL at a 530 nm emission peak. With the pressure increasing in a region of 0–1.50 GPa, a slight red shift of peak wavelength gradually occurs. When the applying pressure increases up to 2.0 GPa (Fig. S8), the PL suddenly quenches,

which is followed by a large peak displacement, and a blue shift occur in 560–580 nm under increasing pressure to 13.3 GPa. The PL photographs obviously exhibit that bright green PL of CPB NC fades away and transforms into a bluish white state from pressure of 0 GPa to 13.3 GPa (Fig. 3d). The disappearance of PL spectra at about 2.0 GPa are attributed to the amorphous lattice of CPB NC where the nonradioactive processes improve [33,34]. The piezochromic transition suggests the accomplishment of the IPT in CPB NC through changing the optical properties and structure [31,35]. It is noted that when the pressure is released back to 0 GPa, CPB NC reverts to green PL which is yet quenched to a certain extent compared with the initial PL intensity at 0 GPa. From the fluorescence (FL) spectra and PL spectra under different conditions in Fig. S9, we can find that CPB NC dispersion shows a decreasing FL under ultrasound than that without ultrasound, and the PL intensity as well as the photograph of CPB NC obviously fade away under R0 GPa when contrast to 0 GPa, which is closer to the state at 1.5 GPa. This fully indicates that after applying pressure to CPB NC and returning to the non-pressure state, the material structure does not completely return to the original state, revealing an irreversible IPT of CPB NC under high pressure. This result is exactly consistent with the phenomenon that the lattice fringes and crystal plane exposure of CPB NC change before and after applying ultrasound. Fig. 3e exhibits that the PL intensity decreases with magnifying pressure, which is originated from the high degree of distortion and random orientations of octahedra in CPB NC under deviatoric stress [33,34]. When the trend of PL peak

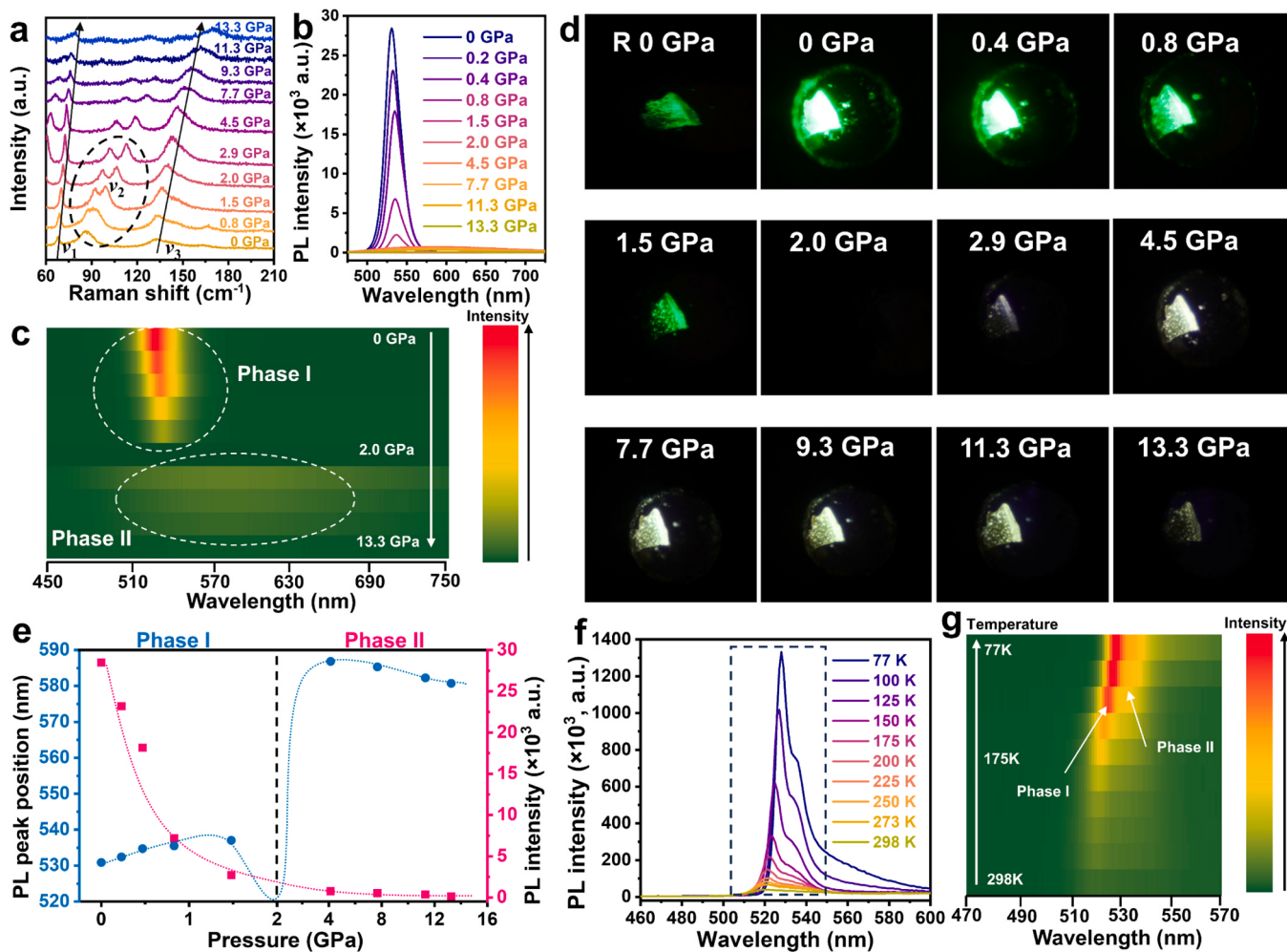


**Fig. 3.** (a) *In-situ* pressure-dependent Raman and (b-c) PL spectra of CPB NC. (d) Pressure-dependent PL photographs of CPB NC (R 0 means the pressure is released back to 0 GPa). (e) PL peak position and PL intensity at various pressure levels. (f-g) The temperature-dependent PL spectra of CPB NC.

position shows a turning point at 2.0 GPa, the occurrence of the isostructural transition of orthorhombic phase I to phase II at this condition can be predicted. The agreement of pressure-dependent Raman and PL spectra allow us to believe that introducing pressure results in an IPT over CPB NC, which succeeds to break asymmetry of original orthorhombic phase in CPB NC. Temperature-dependent photoluminescence (TD-PL) spectra were measured to reveal the interior change of CPB NC (Fig. 3f). The peak wavelength and intensity both increase when the temperature decreases from 298 K to 77 K, along with splitting of the primary peak (Fig. 3g). Such a peak splitting can also be considered to be the result of phase transition of CPB NC. According to reported studies [16,17,36], traditional CPB QDs with cubic phase is converted to an orthorhombic phase (*Pna2*<sub>1</sub>) which is a non-centrosymmetrical structure below 278 K to complete a nonpolar-to-polar phase transition and obtain piezoelectricity. For CPB NC, a cooling treatment is also able to transform the non-centrosymmetrical phase to another distorted structure *via* disrupting the asymmetrical balance. In a similar fashion, pressure induces the irreversible IPT within CPB NC, which can speculate to breaking the asymmetrical structure for shift of positive and negative charge center to possess permanent piezoelectricity for building polarization electric-field.

To reveal the specific change of the IPT, we simulated the crystal change of CPB NC at different pressure states based on MedeA-VASP. Firstly, a smaller angle of Pb-Br-Pb reflects a stronger tilting degree of [PbBr<sub>6</sub>]<sup>4-</sup> octahedra in CPB NC under 2 GPa (Fig. S10). Fig. 4a shows that the Pb-Br network distorts after applying pressure of 2 GPa. From

the view of *c*-axis direction, the adjacent Br-Pb-Br angles using Pb<sup>2+</sup> as the hinge center have sharpening (90.59° to 90.238°) and passivation (89.328° to 89.762°) from the ambient condition to 2 GPa state. Simultaneously, Pb-Br bond shrinks with increased pressure, including a compression of bond length from 3.08 to 3.03 Å. The center location of Cs<sup>+</sup> also owns displacement on the direction of *a*-axis and *b*-axis (Table S1). Although the changed CPB NC under pressure is still belong to orthorhombic phase, this IPT tilts and distorts [PbBr<sub>6</sub>]<sup>4-</sup> octahedra with shortening length of Pb-Br bond, enabling CPB NC to break asymmetry balance for the non-overlapping of positive and negative ion centers, which is a fundamental of piezoelectric property.

The piezoelectric response of CPB NC can be well observed by a piezo-response force microscopy (PFM). Firstly, atomic force microscopy (AFM) was measured and gave the morphology information of CPB NC (Fig. S11). Then, PFM curves are displayed in Fig. 4b. Employing 10 V voltage as oscillation signals source of the cantilever to the CPB NC reads out a piezoelectric amplitude signal, manifesting an obvious butterfly-shaped appearance. Local polarized electric-field loops (P-E) of the CPB NC also present a clear hysteresis with 180° phase switching. Besides, the resonant peaks under different excited voltages were recorded (Fig. 5a). CPB NC possesses distinct resonant peaks at about 225 kHz due to the piezoelectric vibration excited by voltage, depicting a prominent linear correlation of amplitude (Fig. 5b). This confirms a linear piezoelectricity of the as-synthesized CPB NC [37].

Furthermore, the amplitude and phase response images tested by

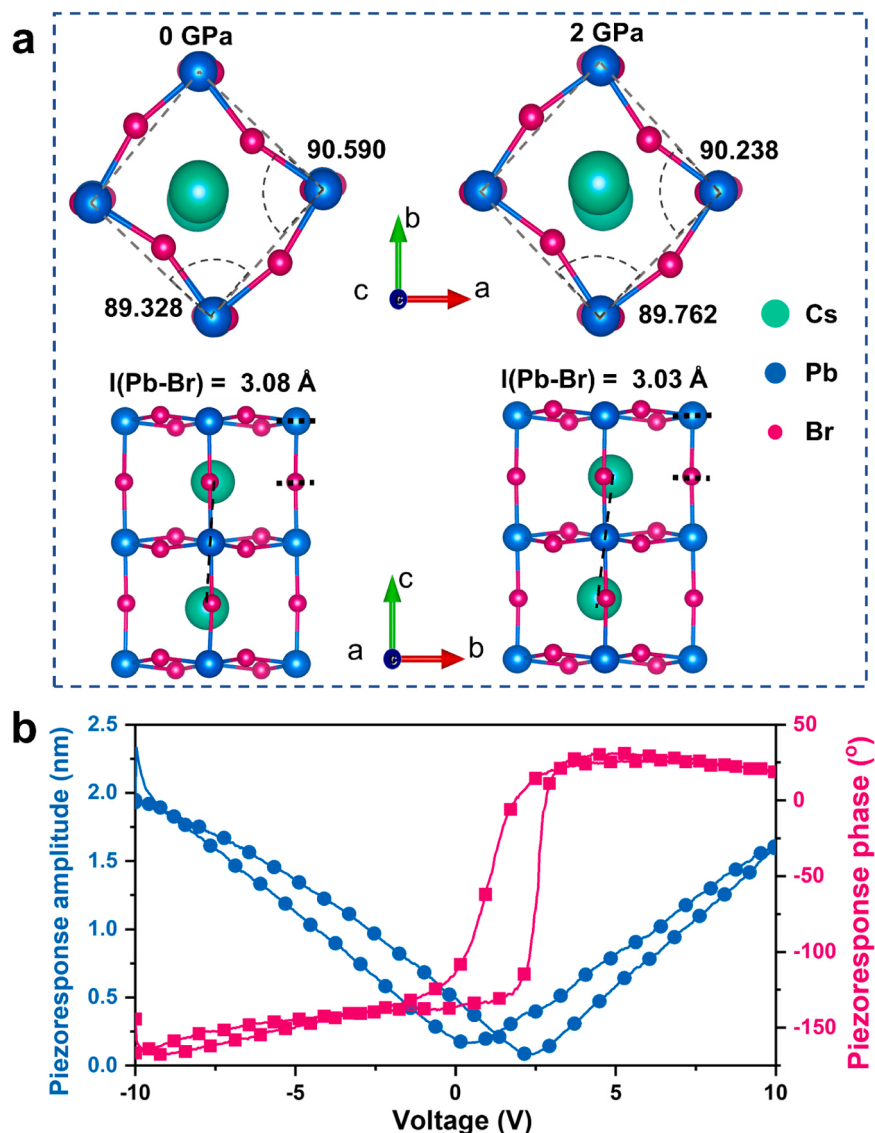


**Fig. 4.** (a) Pb–Br network structure of CPB NC viewed along *c* and *a* axis at two pressure states. (b) Amplitude butterfly (blue) and phase hysteresis loop (pink) of CPB NC.

PFM are exhibited in Fig. 5c and d. The domain distribution of CPB NC has a clear gradient that reflects a good longitudinal piezoelectric response. Based on above results, pressure induces the IPT within CPB NC to tilt the  $[\text{PbBr}_6]^{4-}$  octahedron with shift of  $\text{Cs}^+$ , breaking the asymmetrical structure for shift of positive and negative charge center to form piezoelectricity.

### 3.3. Band positions of CPB NC with IPT-induced piezoelectricity

The procedure of thermodynamics feasibility towards catalysis is dependent on the band position of semiconductor catalysts. We then investigated the energy band structure of CPB NC under different pressure by *in-situ* pressure-dependent absorption spectra and density functional theory (DFT). As depicted in Fig. 5e and Fig. S12, the absorption edge of CPB NC is about 570 nm at ambient condition, revealing 2.30 eV band gap of CPB NC. The absorption edge firstly has a slight red shift accompanied by the narrowing down of band gap when the applying pressure increases. There is a sharp blue shift at the absorption edge that means a turning trend of band gap value at about 2 GPa, which is ascribed to the IPT in CPB NC under this pressure state [31]. After the applied pressure is released back to the ambient condition, the

absorption spectrum of CPB NC basically recovers and the band gap rebounds to about 2.32 eV. However, as mentioned above, this is not a complete reversible IPT process, so the band gap and absorption spectrum of CPB NC do not completely return to the initial state. In total density of states (TDOS), the valence band maximum (VBM) of CPB NC under 2 GPa pressure is closer to Fermi level than that at 0 GPa (Fig. S13), which reflects the band gap decreases under 2 GPa pressure and is consistent with 2.25 eV of band gap at 2 GPa from Fig. S12. The partial DOS (PDOS) shown in Fig. S14 elucidates that the conduction band (CB) bottom primarily originates from p orbitals of Pb, and the top of valence band (VB) is mainly contributed by Br p orbitals. Furthermore, the p orbital of Cs forms narrow bands at deep energy values of  $-8.06$  eV under 0 GPa pressure, and the energy value changes to  $-8.80$  eV under 2 GPa pressure, which verifies the generation of new orthorhombic phase in CPB NC [38].

Based on DFT simulation, computational band gaps of CPB NC under different pressures possess the same trend of change with the measured band gaps above (Fig. S15). It is noted that the energy band gap of CPB NC changes from direct to indirect, and then returns to direct state with increasing pressure from 0 to 2 GPa. This is probably caused by the change in the frequency and direction of the lattice vibration due to the

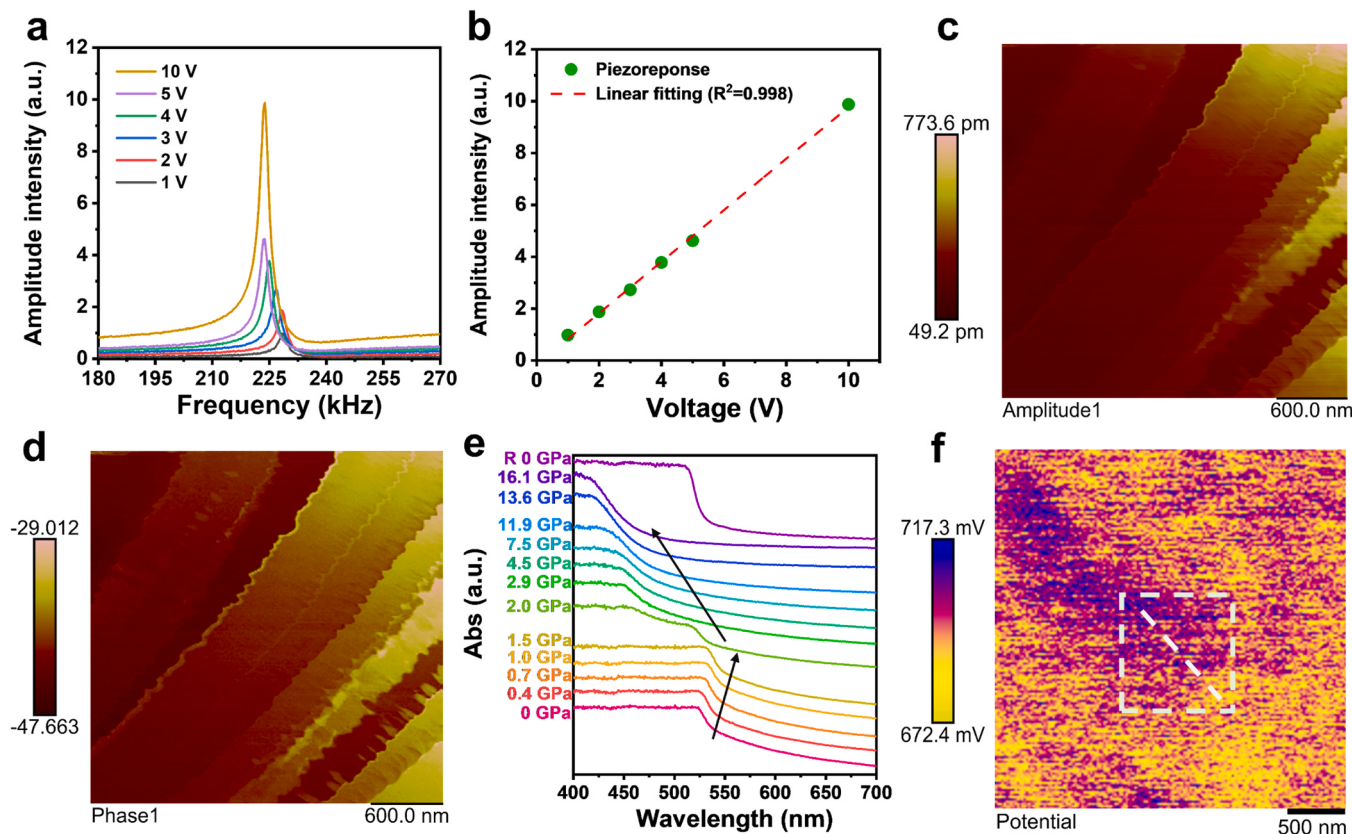


**Fig. 5.** (a) Resonant peaks under different external voltages on CPB NC. (b) Linear fit of the amplitude intensity with applying voltages over CPB NC. The (c) amplitude and (d) phase response image of CPB NC tested by PFM. (e) *In-situ* pressure-dependent absorption spectra of CPB NC. (f) Contact potential difference of CPB NC measured by KPFM.

pressure. This change also indirectly confirms that the pressure-induced phase transition in CPB NC does exist. In addition, introducing pressure vibration enables a band tilting of CPB NC. In the common UV-Vis diffuser reflectance (DRS) spectra and its calculated Tauc's curve (Fig. S16a and b), the value of CPB NC band gap is 2.30 eV, which is matched well with the results of *in-situ* pressure-dependent absorption spectra. Mott-Schottky plots of CPB NC with and without ultrasonic vibration were tested, showing the primordial band position of CPB NC where CBM is  $-0.80$  V and valence band maximum (VBM) is  $1.50$  V (Fig. S16c). During the ultrasonic vibration process, the CBM and VBM fall to  $-0.95$  V and  $1.30$  V (Fig. S16d), respectively. According to currently recognized mechanism of piezoelectric catalysis [39,40], the tilting of energy band is derived from the high piezoelectric potential generated by the polarized electric-field in the piezoelectric materials. Therefore, the contact potential difference (CPD) between CPB NC and probe tip was measured through Kelvin probe force microscopy (KPFM). As illustrated by Fig. 5f, CPB NC owns the highest CPD of 711 mV approximately. The average CPD of the nanocube region with the greatest difference in height crossed by a dash line can reach 700 mV (Fig. S17). COMSOL Multiphysics were also used to simulate surface piezoelectric potential of CPB NC. Fig. S18 displays a low surface potential of CPB NC at ambient condition, and there is no significant gradient of potential. When 2 GPa pressure were employed, the surface potential of CPB NC was improved. The maximum difference of piezoelectric potential on the surface of CPB NC achieved 0.9 V and surpassed the required redox potential of the most redox reactions. Such a high piezoelectric potential produced by pressure are able to cause the band tilting of CPB NC which provides excited carriers (electrons and holes) with sufficient energy for redox reactions (Fig. S19).

Nevertheless, previous reports pointed out that applying unidirectional pressure would lead to the directional accumulation of free

carriers on the two polar sides, forming a depolarization field. A static charge balance happens because of the depolarization field, which not only shields the polarized electric-field by screening charges from electrolyte, but also screens the band tilting [41]. Consequently, employing pressure with periodic variation is essential to prevent the generation of depolarization field, and the ultrasonic vibration is a classical periodic stress.

#### 3.4. IPT-induced piezoelectric catalytic $\text{CO}_2$ reduction

In accordance with above findings, we focus on the performance of piezoelectric catalytic  $\text{CO}_2$  reduction using as-prepared CPB NC under ultrasonic vibration. A ultrasonic cleaner was utilized to provide ultrasonic vibration of 40 kHz frequency that gives about 2 GPa stress via bubble cavitation to induce the IPT for piezoelectric polarization of CPB NC [42,43]. We firstly evaluated activities of piezoelectric catalytic  $\text{CO}_2$  reduction with different dosages of CPB catalysts. As shown in Fig. 6a, yields of  $\text{CO}_2$  reduction products rises and then declines with improving CPB NC dosage. Usually, a higher dosage of CPB NC leads to more piezoelectric carriers for catalytic reaction, so that  $0.5 \text{ g L}^{-1}$  CPB NC presents the optimal piezoelectric catalytic activity to generate  $\text{CH}_4$  ( $21 \mu\text{mol g}^{-1}$ ) and  $\text{CO}$  ( $48 \mu\text{mol g}^{-1}$ ) within 3 h, showing a total electrons consumption (TEC) of  $88 \mu\text{mol g}^{-1} \text{ h}^{-1}$ . Nevertheless, it's difficult for excess CPB NC to be evenly dispersed, which cuts down the fixed vibration pressure to lessen the piezoelectric carriers. [20] The ultrasonic power determines the magnitude of applied vibration amplitude. It's apparent that pure stirring (0 W) without ultrasound fails to generate catalytic activity using CPB NC (Fig. 6b), while the two products increased with an enhancement of ultrasonic vibration power. This proves that only the periodic vibration pressure can alternately change the piezoelectric polarized electric-field to release abundant metastable

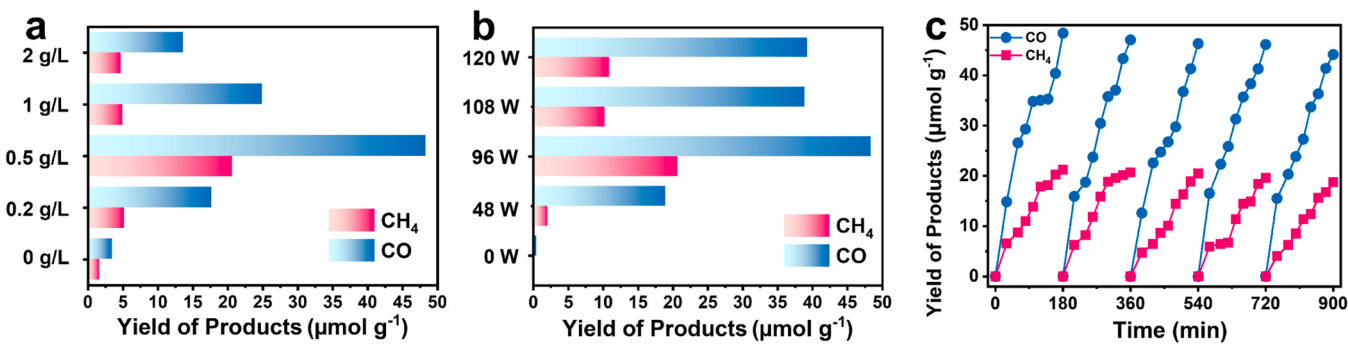


**Fig. 6.** (a) Yield of products in  $\text{CO}_2$  reduction with different dosage of CPB NC within a 3-h reaction. (b) The influence of ultrasonic power for  $\text{CO}_2$  reduction within a 3-h reaction. (c) Cycle runs of piezoelectric catalytic  $\text{CO}_2$  reduction. Reaction conditions: ultrasonic power = 96 W, vibration frequency = 40 kHz, temperature at  $25\pm1$  °C.

carriers for catalytic reactions. The power of 96 W with 40 kHz frequency is the best ultrasonic condition, indicating that the vibration condition contributes to reaching saturated piezoelectric electrons density. Under higher power of the ultrasonic vibration (108 and 120 W), the efficiency of piezoelectric catalytic  $\text{CO}_2$  reduction falls instead. As we all know, ultrasonic power determines the amplitude of ultrasonic vibration. Although an increase in ultrasonic power can improve the intensity of the ultrasonic force, the higher force would lead to larger cavitation bubbles generated near the surface of materials, thereby reducing the numbers of bubbles and implosion. Therefore, the piezoelectric catalytic performance of CPB NC reduced under excessive ultrasonic power. This would be further explained in the mechanism

part below.

A cyclic experiment was conducted to appraise the piezoelectric catalytic stability of CPB NC. As displayed in Fig. 6c, CPB NC was used to carry out a 15-h cyclic test. Used CPB NC was extracted and washed via centrifugation for following cyclic experiments, exhibiting that yields still achieved as high level as  $18.7 \mu\text{mol g}^{-1}$  of CH<sub>4</sub> and  $44 \mu\text{mol g}^{-1}$  of CO after 15 h. From the TEM images of CPB NC after cycle test of piezoelectric catalytic  $\text{CO}_2$  reduction (Fig. S20), we can find that CPB NC still keeps a stable cube shape after a long-time ultrasonic reaction. The lattice fringe of CPB NC is consistent with Fig. 1h above. The result indicates an outstanding stability of morphology structure and reusability of the as-prepared CPB NC in the piezoelectric catalytic process. By

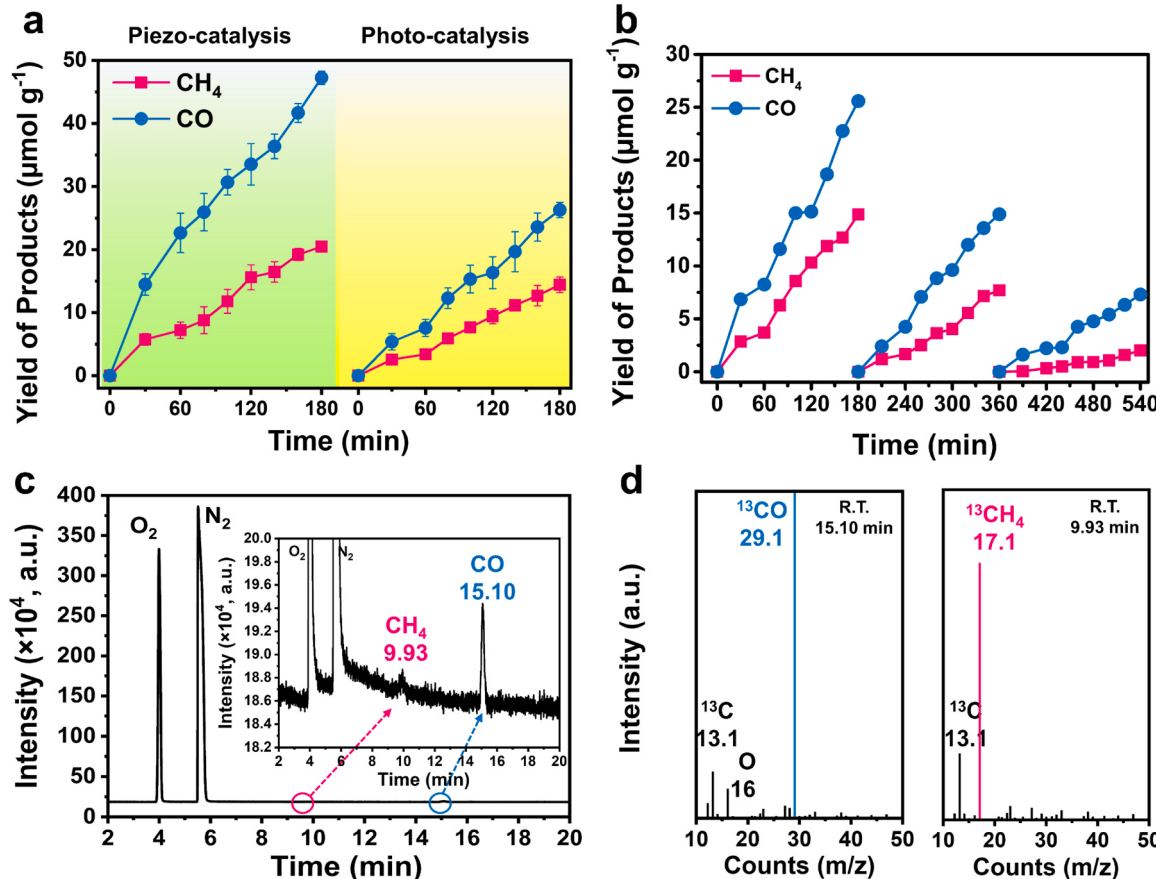


**Fig. 7.** (a) The efficiency of piezoelectric- and photo-catalytic  $\text{CO}_2$  reduction over CPB NC. (b) The stability of photocatalytic  $\text{CO}_2$  reduction with CPB NC. (c) Total ion chromatographic (TIC) patterns over CPB NC for <sup>13</sup>CO<sub>2</sub> piezoelectric catalytic reduction. (d) GC-MS of CH<sub>4</sub> and CO in the isotope experiment with <sup>13</sup>CO<sub>2</sub> as gas source for piezoelectric catalytic reaction.

contrast, the efficiency of photocatalytic  $\text{CO}_2$  reduction using CPB NC ( $14 \mu\text{mol g}^{-1} \text{CH}_4$ ,  $25 \mu\text{mol g}^{-1} \text{CO}$ ,  $54 \mu\text{mol g}^{-1} \text{h}^{-1} \text{TEC}$ ) are much less than that of piezoelectric catalysis during a 3-h reaction, manifesting that CPB NC has a higher piezo-catalytic activity instead of photo-driven process (Fig. 7a). Unsurprisingly, CPB NC is unable to maintain a long-period stability by means of photo-catalytic procedure, which displays inappreciable yield of reduction products after 3 cycles (Fig. 7b). Additionally, a comparison of the performance of catalytic  $\text{CO}_2$  reduction systems by different kinds of all-inorganic perovskites and piezoelectric catalysts has been summarized and listed in Table S2. CPB NC exhibits a superior piezoelectric catalytic performance for  $\text{CO}_2$  reduction to C1 products with a stable process. The productivities of CO and  $\text{CH}_4$  and the TEC in the vibration-introduced piezoelectric catalysis outperform the most of reported  $\text{CO}_2$  reduction systems by state-of-the-art halide perovskites and piezoelectric catalysts. This sets the tone for a trend of replacing traditional photocatalysis with piezoelectric catalysis using CPB.

We also used isotopically labeled  $^{13}\text{CO}_2$  (99.999 %) gas as the carbon source and confirmed the source of  $\text{CH}_4$  and CO. The isotope-labeling experiment was carried out with injecting  $^{13}\text{CO}_2$  instead of common  $\text{CO}_2$ . The detection of  $^{13}\text{CH}_4$  and  $^{13}\text{CO}$  was conducted using a gas chromatograph mass spectrometer (GC-MS). The result of total ion chromatogram (TIC) is exhibited as Fig. 7c. Peaks located at 9.93 and 15.10 min are assigned to signals of  $\text{CH}_4$  and CO, demonstrating the formation of these two products in  $\text{CO}_2$  conversion. The GC-MS (Fig. 7d) shows two primary signals at  $m/z = 17.1$  ( $^{13}\text{CH}_4$ ) and  $m/z = 29.1$  ( $^{13}\text{CO}$ ).  $^{13}\text{CH}_4$  and  $^{13}\text{CO}$  signals are broken into two other fragments at  $m/z = 13.1$  ( $^{13}\text{C}$ ) and  $m/z = 16$  (O), which suggests that  $\text{CH}_4$  and CO certainly originate from piezoelectric catalytic  $\text{CO}_2$  reduction over CPB NC.

In principle, catalytic  $\text{CO}_2$  reduction reactions rely on activated electrons generated by piezoelectric catalysts. In order to prove the generation of piezoelectric electrons on CPB NC, a series of experiments including hydrogen ( $\text{H}_2$ ) evolution and organic dye degradation were performed. CPB NC produce  $\text{H}_2$  at a yield of  $\sim 120 \mu\text{mol g}^{-1}$  with a steady upward trend in 3 h (Fig. 8a), while the reaction system without

catalyst generates negligible  $\text{H}_2$  via ultrasonic cavitation. As described in Fig. S21, compared with the reaction systems with CPB NC, there is negligible yield of gas products in the absence of CPB NC within the reaction systems, which fully demonstrates the  $\text{H}_2$ ,  $\text{CH}_4$  and CO are derived from piezoelectric catalytic reduction reactions by CPB NC instead of the decomposition of ethyl acetate.

In the meanwhile, Fig. 8b displays RhB degradation rates in different systems based on RhB absorbance in Fig. S22. The results demonstrate that CPB NC can efficiently produce reactive oxygen species (ROS) by combination of  $\text{O}_2$  and piezoelectric carriers to decompose organic dye. The measurement of electron paramagnetic resonance (EPR) proves the existence of ROS. It can be seen from Fig. 8c that CPB NC exhibits a characteristic peak of superoxide radicals ( $\text{O}_2^\bullet$ ) through DMPO trapping agent under ultrasonic vibration. Prolonging vibration time makes the signal of  $\text{O}_2^\bullet$  become stronger. It's proverbial that  $\text{O}_2^\bullet$  is derived from the reduction of oxygen ( $\text{O}_2$ ) via attack of piezoelectric electrons ( $e^-$ ), the specific mechanism of  $\text{H}_2$  production and ROS generation for RhB degradation are described as following equations (Eqs. 1–3) [44]:



To reveal migration of piezoelectric carriers of as-prepared CPB NC, the transient piezoelectric current response is depicted in Fig. 8d, manifesting obvious and repeatable piezo-current signals with on/off of applying ultrasound. The trend of maximum current density ( $j$  difference) increases and then declines with ultrasonic power raising, and 96 W power of ultrasonic vibration provides CPB NC with the highest migration rate of carriers (current density =  $0.28 \mu\text{A cm}^{-2}$ ). The result is matched well with the piezoelectric catalytic  $\text{CO}_2$  reduction. The electrochemical impedance spectroscopy (EIS) and fluorescence (FL) spectra of CPB NC further explain a high-efficient carriers transfer under ultrasonic vibration (Figs. S23 and S24, Table S4).

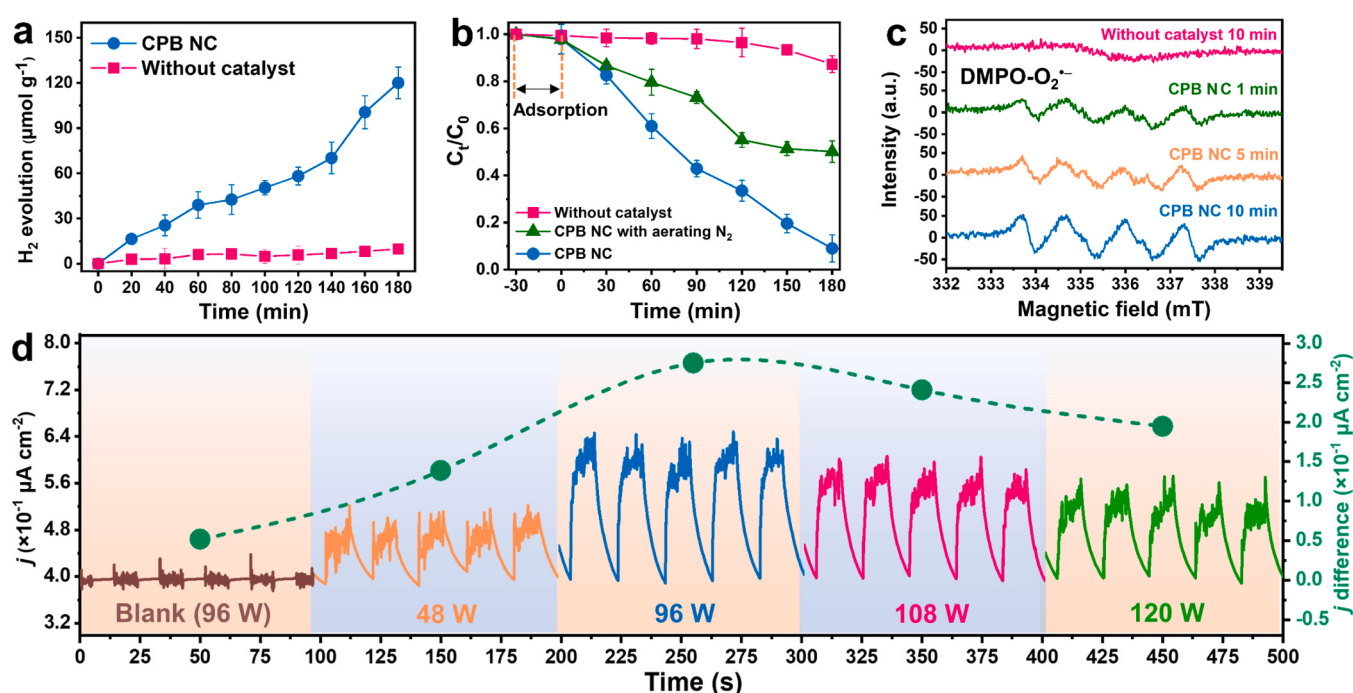


**Fig. 8.** (a)  $\text{H}_2$  production with time increasing under ultrasonic vibration. (b) RhB degradation using CPB NC with different condition. (c) EPR signals of  $\text{O}_2^\bullet$  under ultrasonic vibration at different time. Reaction conditions: ultrasonic power = 96 W, vibration frequency = 40 kHz, temperature at  $25 \pm 1^\circ\text{C}$ . (d) Transient piezoelectric current response under different ultrasonic power.

### 3.5. Mechanism of piezoelectric catalytic $\text{CO}_2$ reduction over CPB NC

How does the IPT-induced piezoelectricity of CPB NC work for catalytic  $\text{CO}_2$  conversion? Combined with above discussions, introducing adequate pressure enables CPB NC to carry out the IPT that accompanies non-overlapping of positive and negative ion center. This IPT-induced asymmetry breaking builds a polarized piezoelectric-field in CPB NC which possesses a high potential (0.9 V) for energy band tilting. Then, excited carriers including  $e^-$  and holes ( $h^+$ ) are efficiently separated and endowed with high energy by band tilting to reach redox potential levels. This leaves a key issue as to how the piezoelectric  $e^-$  is excited in the ultrasonic piezoelectric-catalysis. Based on reported research, the sound pressure fluctuates in a form of wave during the propagation of ultrasonic waves in a fluid [45,46]. A scheme is shown in Fig. S25 that water molecules go through a process of ultrasonic cavitation where they can be squeezed out in the positive phase of the pressure (compression) and then disintegrated in the negative phase (decompression). According to reported research [43], the total pressure ( $P$ ) in a cavitation bubble is derived from following equation:  $P = p_0 + 2\sigma/R_0$ , where  $p_0$  is the disturbed pressure,  $\sigma$  is the surface tension and  $R_0$  is the initial bubble radius. Under the calculating conditions that temperature ( $T_0$ ) = 298 K,  $p_0$  = 1 atm, and  $R_0$  = 50  $\mu\text{m}$ , the released pressure inside a bubble in n-dodecane can reach up to 0.1–1 GPa at the acoustic frequency of 19.5 kHz and acoustic pressure amplitude of 1.3 atm. Therefore, such an alternate cyclic-procedure results in the formation and growth of cavitation bubbles, which is able to release a huge impact force as high as 0.1–1 GPa to provide sufficient energy for  $e^-$  excitation when the cavitation bubbles implode at a critical size [43,47]. Significantly, the vibration offered by our experimental ultrasound (frequency of 40 kHz and power of 96 W) and theoretical simulation can reach about 2 GPa pressure that sufficiently allows CPB NC to excite  $e^-$  from the VBM. It is noted that although an increase in ultrasonic power can improve the intensity of the ultrasonic force, the higher force would lead to larger cavitation bubbles generated near the surface of materials, thereby reducing the numbers of bubbles and implosion. Because the pressure on the material comes from the pressure released by the implosion of cavitation bubbles, the number of bubble implosion decreasing would lead to a decreasing for the times of the material

receiving ultrasonic pressure. Therefore, the piezoelectric catalytic performance of CPB NC reduced under excessive ultrasonic power. Too small an ultrasonic power will reduce the pressure released by the implosion of cavitation bubbles, thereby weakening the IPT-induced piezoelectricity of CPB NC. So, there will be an optimal ultrasonic power to achieve the best ultrasonic piezoelectric performance by CPB NC.

Combined with the above, the entire piezoelectric process in CPB NC is shown as Fig. S26. Under the induction of IPT by pressure, bound charges within CPB NC migrate in opposite directions to create a built-in polarizing electric field with a high potential. At the same time, the vibration pressure as high as 2 GPa also stimulates the internal  $e^-$  excitation of CPB NC. The polarizing electric field not only leads to the energy band tilting for  $e^-$  reaching the ideal redox potential, but also successfully separates  $e^-$  and  $h^+$  towards opposite sides of CPB NC by bound charges to avoid recombination of electron-hole pairs.

To explore the  $\text{CO}_2$  reduction reaction followed by the excitation of piezoelectric  $e^-$  on CPB NC, electron states and the transfer process are investigated. X-ray photoelectron spectroscopy (XPS) is used to analyze the element and electrons state of CPB NC (Fig. S27), and difference of charge density is utilized to elucidate the electrons transfer in the catalytic  $\text{CO}_2$  reduction. Fig. 9a displays that CPB NC adsorbs the  $\text{CO}_2$  and exhibits an even-distributed electron cloud around the  $\text{Cs}^+$  and  $\text{Br}^-$  at the 0 GPa. The  $\text{CO}_2$  maintains a stable liner structure (bond angle=185.42°) with adsorption energy of 0.34 eV. After employing pressure, a large number of  $e^-$  transfer rapidly owing to the piezoelectric potential of CPB NC, continuing to consume in CPB and accumulate on  $\text{CO}_2$ , and shows a dense electron cloud. The adsorbed  $\text{CO}_2$  is activated through receiving electrons and transformed into a bent structure (bond angle=152.77°) that is easy to break bonds [48]. The adsorption energy also improves to 0.58 eV, leading to a stronger combination of  $\text{CO}_2$  and CPB NC under pressure. The electronic local function (ELF) map is simulated to reveal distribution profiles of  $e^-$ , which microscopically confirms that CPB has a more intensive bonding with  $\text{CO}_2$  under 2 GPa compared with that at the ambient state. In other words, the stress provided by ultrasonic vibration in the actual reaction not only made CPB NC generate abundant  $e^-$  by IPT process, but also improved  $\text{CO}_2$  adsorption energy for bonding with CPB NC and exciting  $\text{CO}_2$  by

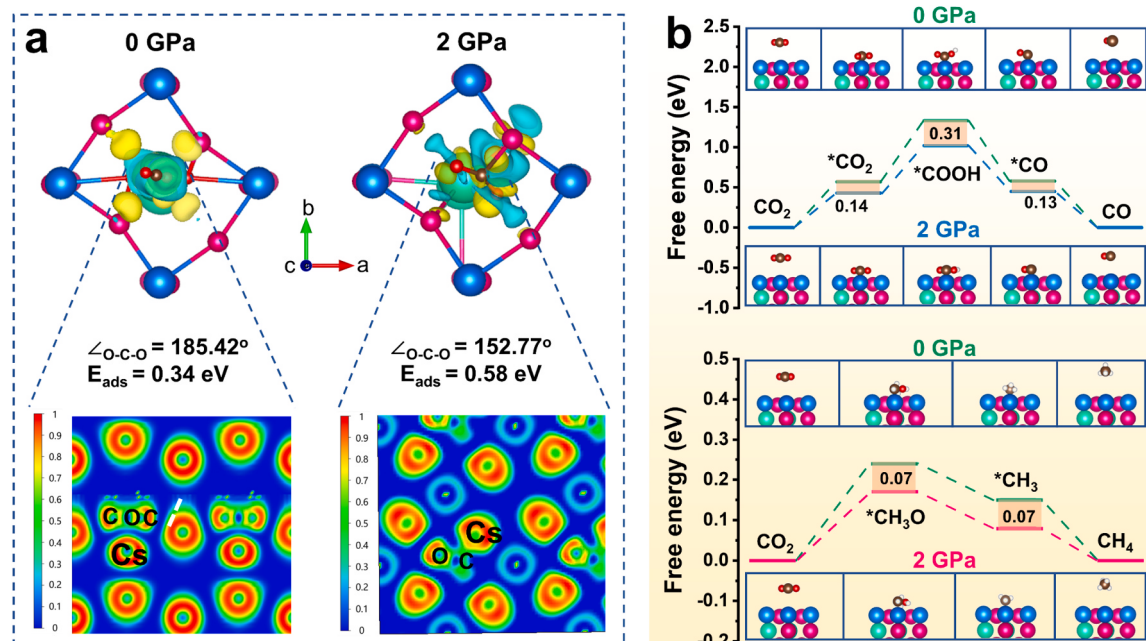
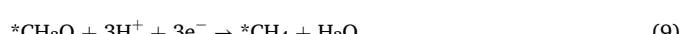


Fig. 9. (a) The charge density difference and ELF map of CPB NC with adsorbing  $\text{CO}_2$  (Electron accumulation and depletion are marked in cyan and yellow agglomerates, respectively). (b) The difference of  $\text{CO}_2$  reduction pathways with configurations of intermediates on CPB NC under two pressure conditions. (Cyan, blue, pink, red, grey and white spheres refer to  $\text{Cs}$ ,  $\text{Pb}$ ,  $\text{Br}$ ,  $\text{O}$ ,  $\text{C}$  and  $\text{H}$  atoms, respectively).

transferred  $e^-$ . Besides, Cs atom owns a high degree of electrons localized and the highest  $\text{CO}_2$  adsorption energy (Fig. S28), which can act as a reactive site to combine with C atoms, contributing to adsorption and bond breakage of  $\text{CO}_2$  [49].

We then explored pathways and intermediate products of piezoelectric catalytic  $\text{CO}_2$  reduction on CPB by DFT calculation (Fig. 9b). In the first place, the  $\text{CO}_2$  molecule were adsorbed and activated on CPB, which was followed by proton-coupled electron transfer processes to generate different mid-products. The first proton-coupled electron-transfer step where the  $^*\text{CO}_2$  transformed to  $^*\text{COOH}$  was a rate-determining step of generation of CO.  $^*\text{CH}_3\text{O}$  was then formed in the fifth proton-coupled electron-transfer process, which was the rate-determining step for  $\text{CH}_4$  [50]. In contrast to the condition of 0 GPa, free energy of different intermediate products in the CO and  $\text{CH}_4$  generation is 0.31 eV and 0.07 eV lower under 2 GPa stress over the CPB NC. The decreased energy illustrates the advantage of applying pressure to break the C=O bond of  $\text{CO}_2$ , which reduces the energy barrier of  $\text{CO}_2$  conversion to  $\text{CH}_4$  and CO [51]. The detailed  $\text{CO}_2$  reduction pathways are described as equations (Eqs. 4–10) below:



The asterisk represents substrates where molecules or transition

states species adsorbed on.

Fig. 10 proposes an entire principle of piezoelectric catalytic  $\text{CO}_2$  conversion over CPB NC. When a mechanical pressure is applied as high as 2 GPa, the tilt and distortion of  $[\text{PbBr}_6]^{4-}$  octahedrons induce the IPT to transform from orthorhombic phase (phase I) to a new orthorhombic phase (phase II) of CPB NC. Such an IPT process results in smaller Pb-Br-Pb angles and shorter Pb-Br bonds, along with a stronger shift of central  $\text{Cs}^+$ , which breaks the asymmetry of CPB NC. The piezoelectric polarization occurs by the asymmetry breaking, which could polarize bound charges to form a strong polarized electric-field with high piezoelectric potential. Therefore, carriers ( $e^-$  and  $\text{h}^+$ ) excited by the high pressure are efficiently separated by the polarized electric-field and avoided recombination. Simultaneously, the presence of high piezoelectric potential tilts energy bands of CPB NC by negative shift of the CB edge, giving high energy to carriers. In this way, the high-energy  $e^-$  can migrate to the reactive site Cs atom for following  $\text{CO}_2$  reduction.  $\text{CO}_2$  molecules are adsorbed on the surface of CPB NC and was then activated to be a bent geometry by  $e^-$  flowed from the Cs atom under pressure. The bent  $\text{CO}_2$  is easily to break C=O bonds, and then reacts with  $e^-$  to produce  $\text{CH}_4$  and CO by proton-coupled electron-transfer processes, realizing a high efficiency of piezoelectric catalytic  $\text{CO}_2$  reduction. After releasing mechanical stress, CPB NC would not return to its original state but maintain the phase II for the next cyclic reaction. It's worth noting that this irreversible phase transition endows the CPB NC material permanent piezoelectric properties, achieving a persistent piezoelectric polarization for catalysis with CPB NC. Unlike the photocatalysis where photons directly excite electron-hole pairs that are easy to recombine after separation, under the action of an alternating pressure field,  $e^-$  and  $\text{h}^+$  can be continuously generated and separated, effectively inhibiting their recombination. At the same time, according to the transient current characterization (Fig. S29), the electron transfer efficiency of CPB NC under light is not as good as that under piezoelectricity of ultrasound.

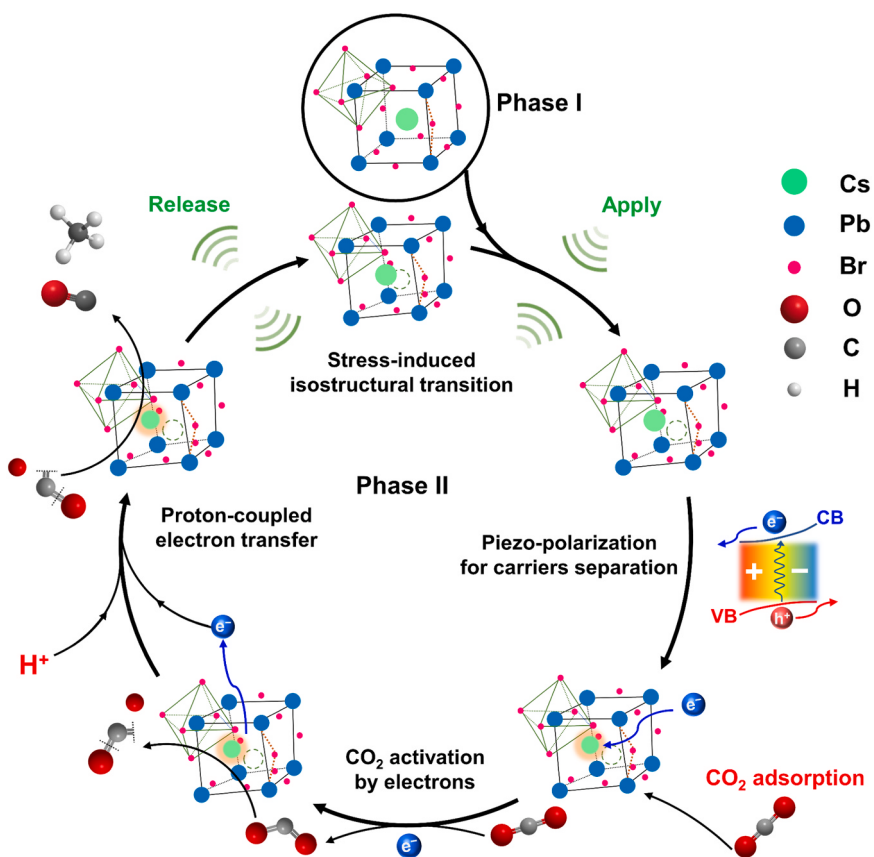


Fig. 10. Mechanism of piezo-catalytic  $\text{CO}_2$  reduction over CPB NC under stress.

These results fully explain that the efficiency and stability of photo-catalytic  $\text{CO}_2$  reduction using CPB NC are poorer than that of piezoelectric catalysis.

#### 4. Conclusion

To conclude, a nanocube-like  $\text{CsPbBr}_3$  (CPB NC) was prepared and employed into piezoelectric catalytic  $\text{CO}_2$  reduction under pressure vibration. The dramatical piezoelectricity is profited from an isostructural phase transition of orthorhombic phase I to orthorhombic phase II (IPT) to break asymmetry of crystal structure in CPB NC under mechanical pressure, specifically manifested as contraction of  $\text{Pb}-\text{Br}$  bond and displacement of center  $\text{Cs}^+$ . This forms a polarized electric-field with high piezoelectric potential for band tilting to provide abundant high-energy electrons. Experimental and DFT results demonstrate that IPT-induced piezoelectricity of CPB NC benefits for the activation of  $\text{CO}_2$  via piezoelectric electrons, that enhances adsorption energy of  $\text{CO}_2$  and decreases energy barrier of  $\text{CO}_2$  reduction reaction, collectively contributing to an excellent performance of  $\text{CO}_2$  catalytic conversion. The study reveals that IPT can act as a new strategy to endow all-inorganic halide perovskites—CPB with piezoelectricity, which present a more efficient catalytic approach for  $\text{CO}_2$  reduction using piezoelectric effect than photocatalysis. It is expected to inspire the further development of all-inorganic halide perovskites with polar properties by phase transition engineering for energy storage and conversion.

#### CRediT authorship contribution statement

**Jie He:** Writing – original draft, Validation, Methodology, Investigation, Formal analysis. **Xuandong Wang:** Investigation, Formal analysis. **Mingshan Zhu:** Writing – review & editing, Supervision, Funding acquisition, Conceptualization. **Kai Wang:** Investigation, Formal analysis. **Bo Zou:** Writing – review & editing, Methodology. **Pengju Feng:** Writing – review & editing, Validation, Methodology. **Yingtang Zhou:** Writing – review & editing, Methodology, Formal analysis.

#### Declaration of Competing Interest

The authors declare that they have no known competing financial interests or personal relationships that could have appeared to influence the work reported in this paper

#### Data availability

Data will be made available on request.

#### Acknowledgements

This research has been supported by the Guangdong Basic and Applied Basic Research Foundation (No. 2020B1515020038) and the Pearl River Talent Recruitment Program of Guangdong Province (2019QN01L148).

#### Appendix A. Supporting information

Supplementary data associated with this article can be found in the online version at [doi:10.1016/j.apcatb.2024.124186](https://doi.org/10.1016/j.apcatb.2024.124186).

#### References

- [1] N. Uddin, H. Zhang, Y. Du, G. Jia, S. Wang, Z. Yin, Structural-phase catalytic redox reactions in energy and environmental applications, *Adv. Mater.* 32 (2020) 1905739.
- [2] T. Rao, H. Wang, Y.J. Zeng, Z. Guo, H. Zhang, W. Liao, Phase transitions and water splitting applications of 2D transition metal dichalcogenides and metal phosphorous trichalcogenides, *Adv. Sci.* 8 (2021) 2002284.
- [3] X. Yin, C.S. Tang, Y. Zheng, J. Gao, J. Wu, H. Zhang, M. Chhowalla, W. Chen, A. T. Wee, Recent developments in 2D transition metal dichalcogenides: phase transition and applications of the (quasi-) metallic phases, *Chem. Soc. Rev.* 50 (2021) 10087–10115.
- [4] H. Huang, X. Fan, D.J. Singh, W. Zheng, Recent progress of TMD nanomaterials: phase transitions and applications, *Nanoscale* 12 (2020) 1247–1268.
- [5] R. Yang, Y. Fan, L. Mei, H.S. Shin, D. Voiry, Q. Lu, J. Li, Z. Zeng, Synthesis of atomically thin sheets by the intercalation-based exfoliation of layered materials, *Nat. Synth.* 2 (2023) 101–118.
- [6] Y. Xiao, C. Xiong, M.-M. Chen, S. Wang, L. Fu, X. Zhang, Structure modulation of two-dimensional transition metal chalcogenides: recent advances in methodology, mechanism and applications, *Chem. Soc. Rev.* 52 (2023) 1215–1272.
- [7] A. Dobrovolsky, A. Merdasa, E.L. Unger, A. Yartsev, I.G. Schebykin, Defect-induced local variation of crystal phase transition temperature in metal-halide perovskites, *Nat. Commun.* 8 (2017) 34.
- [8] J. Liu, K. Song, Y. Shin, X. Liu, J. Chen, K.X. Yao, J. Pan, C. Yang, J. Yin, L.-J. Xu, Light-induced self-assembly of cubic  $\text{CsPbBr}_3$  perovskite nanocrystals into nanowires, *Chem. Mater.* 31 (2019) 6642–6649.
- [9] J. Xue, D. Yang, B. Cai, X. Xu, J. Wang, H. Ma, X. Yu, G. Yuan, Y. Zou, J. Song, Photon-induced reversible phase transition in  $\text{CsPbBr}_3$  perovskite, *Adv. Funct. Mater.* 29 (2019) 1807922.
- [10] B.W. Zhang, M.N. Zhu, M.R. Gao, J. Chen, X. Xi, J. Shen, R.F. Feng, N. Semagina, N. Duan, H. Zeng, Phase transition engineering of host perovskite toward optimal exsolution-facilitated catalysts for carbon dioxide electrolysis, *Angew. Chem. Int. Ed.* 62 (2023) e202305552.
- [11] A. Liang, R. Turnbull, C. Popescu, I. Fernandez-Guillen, R. Abargues, P.P. Boix, D. Errandonea, Pressure-induced phase transition versus amorphization in hybrid methylammonium lead bromide perovskite, *J. Phys. Chem. C* 127 (2023) 12821–12826.
- [12] C. Zhu, J. Yang, P. Shan, M.-H. Zhao, S. Zhao, C. Pei, B. Zhang, Z. Deng, M. Croft, Y. Qi, Pressure-induced intermetallic charge transfer and semiconductor-metal transition in two-dimensional  $\text{AgRuO}_3$ , *CCS Chem.* 5 (2023) 934–946.
- [13] J.C. Beimborn, L.R. Walther, K.D. Wilson, J.M. Weber, Size-dependent pressure-response of the photoluminescence of  $\text{CsPbBr}_3$  nanocrystals, *J. Phys. Chem. Lett.* 11 (2020) 1975–1980.
- [14] H. Park, C. Ha, J.-H. Lee, Advances in piezoelectric halide perovskites for energy harvesting applications, *J. Mater. Chem. A* 8 (2020) 24353–24367.
- [15] M.H. Bagheri, A.A. Khan, S. Shahzadi, M.M. Rana, M.S. Hasan, D. Ban, Advancements and challenges in molecular/hybrid perovskites for piezoelectric nanogenerator application: a comprehensive review, *Nano Energy* 120 (2024) 109101.
- [16] X. Li, S. Chen, P.-F. Liu, Y. Zhang, Y. Chen, H.-L. Wang, H. Yuan, S. Feng, Evidence for ferroelectricity of all-inorganic perovskite  $\text{CsPbBr}_3$  quantum dots, *J. Am. Chem. Soc.* 142 (2020) 3316–3320.
- [17] L. Zhu, Y.-C. Wang, D. Li, L. Wang, Z.L. Wang, Enhanced spin-orbit coupled photoluminescence of perovskite  $\text{CsPbBr}_3$  quantum dots by piezo-phototronic effect, *Nano Lett.* 20 (2020) 8298–8304.
- [18] H. Mohapatra, M. Kleiman, A.P. Eser-Kahn, Mechanically controlled radical polymerization initiated by ultrasound, *Nat. Chem.* 9 (2017) 135–139.
- [19] Y. Wang, Y. Xu, S. Dong, P. Wang, W. Chen, Z. Lu, D. Ye, B. Pan, D. Wu, C. D. Vecitis, Ultrasonic activation of inert poly (tetrafluoroethylene) enables piezocatalytic generation of reactive oxygen species, *Nat. Commun.* 12 (2021) 3508.
- [20] J. He, X. Wang, S. Lan, H. Tao, X. Luo, Y. Zhou, M. Zhu, Breaking the intrinsic activity barriers of perovskite oxides photocatalysts for catalytic  $\text{CO}_2$  reduction via piezoelectric polarization, *Appl. Catal. B: Environ.* 317 (2022) 121747.
- [21] Z. Ren, F. Chen, Q. Zhao, G. Zhao, H. Li, W. Sun, H. Huang, T. Ma, Efficient  $\text{CO}_2$  reduction to reveal the piezocatalytic mechanism: from displacement current to active sites, *Appl. Catal. B: Environ.* 320 (2023) 122007.
- [22] S. Chen, P. Zhu, L. Mao, W. Wu, H. Lin, D. Xu, X. Lu, J. Shi, Piezocatalytic medicine: An emerging frontier using piezoelectric materials for biomedical applications, *Adv. Mater.* 35 (2023) 2208256.
- [23] Y. Zhou, H. Dong, Z. Xu, Q. Zha, M. Zhu, Y. Meng, Carbon modification facilitates piezocatalytic  $\text{H}_2\text{O}_2$  production over  $\text{BiOCl}$  nanosheets: Correlation between piezoresponse and surface reaction, *Appl. Catal. B: Environ.* 343 (2024) 123504.
- [24] Z. Li, S. Lan, M. Zhu, Piezoelectricity activates persulfate for water treatment: a perspective, *Environ. Sci. Ecotechnol.* 18 (2024) 100329.
- [25] Y. Bao, K. Xiao, S. Yue, M. Zhang, X. Du, J. Wang, W.-D. Oh, Y. Zhou, S. Zhan, Wastewater decontamination via piezoelectric based technologies: Materials design, applications and prospects, *Surf. Interfaces* 40 (2023) 103107.
- [26] C. Porwal, A. Gaur, V.S. Chauhan, R. Vaish, Enhancing piezocatalytic dye degradation through ball milling-induced polarization in nano bismuth zinc borate, *Surf. Interfaces* 42 (2023) 103391.
- [27] S. Zhang, Z. Xu, T. Ji, Z. Chen, P. Guan, A. Li, D. Jv, T. Liang, Y. Weng, Z. Ao, Weak visible-light photo-piezoelectric synergistic catalyst based on the  $\text{Bi}_2\text{Fe}_4\text{O}_9/\text{Carbon-dots/g-C}_3\text{N}_4$  heterostructure, *Surf. Interfaces* 38 (2023) 102809.
- [28] K. Kubota, Y. Pang, A. Miura, H. Ito, Redox reactions of small organic molecules using ball milling and piezoelectric materials, *Science* 366 (2019) 1500–1504.
- [29] Y. Zhao, Y. Gu, B. Liu, Y. Yan, C. Shan, J. Guo, S. Zhang, C.D. Vecitis, G. Gao, Pulsed hydraulic-pressure-responsive self-cleaning membrane, *Nature* 608 (2022) 69–73.
- [30] L. Rao, Y. Tang, C. Song, K. Xu, E.T. Vickers, S. Bonabi Naghadeh, X. Ding, Z. Li, J. Z. Zhang, Polar-solvent-free synthesis of highly photoluminescent and stable  $\text{CsPbBr}_3$  nanocrystals with controlled shape and size by ultrasonication, *Chem. Mater.* 31 (2018) 365–375.

- [31] L. Zhang, Q. Zeng, K. Wang, Pressure-induced structural and optical properties of inorganic halide perovskite  $\text{CsPbBr}_3$ , *J. Phys. Chem. Lett.* 8 (2017) 3752–3758.
- [32] J.-H. Cha, J.H. Han, W. Yin, C. Park, Y. Park, T.K. Ahn, J.H. Cho, D.-Y. Jung, Photoresponse of  $\text{CsPbBr}_3$  and  $\text{Cs}_4\text{PbBr}_6$  perovskite single crystals, *J. Phys. Chem. Lett.* 8 (2017) 565–570.
- [33] Z. Ma, Z. Liu, S. Lu, L. Wang, X. Feng, D. Yang, K. Wang, G. Xiao, L. Zhang, S. A. Redfern, B. Zou, Pressure-induced emission of cesium lead halide perovskite nanocrystals, *Nat. Commun.* 9 (2018) 4506.
- [34] Y. Wang, X. Liu, W. Yang, T. Wen, L. Yang, X. Ren, L. Wang, Z. Lin, Y. Zhao, Pressure-induced phase transformation, reversible amorphization, and anomalous visible light response in organolead bromide perovskite, *J. Am. Chem. Soc.* 137 (2015) 11144–11149.
- [35] L. Wang, K. Wang, B. Zou, Pressure-induced structural and optical properties of organometal halide perovskite-based formamidinium lead bromide, *J. Phys. Chem. Lett.* 7 (2016) 2556–2562.
- [36] R.E. Cohen, Origin of ferroelectricity in perovskite oxides, *Nature* 358 (1992) 136–138.
- [37] C. Hu, F. Chen, Y. Wang, N. Tian, T. Ma, Y. Zhang, H. Huang, Exceptional cocatalyst-free photo-enhanced piezocatalytic hydrogen evolution of carbon nitride nanosheets from strong in-plane polarization, *Adv. Mater.* 33 (2021) 2101751.
- [38] H.M. Ghaithan, Z.A. Alahmed, S.M. Qaid, M. Hezam, A.S. Aldwayyan, Density functional study of cubic, tetragonal, and orthorhombic  $\text{CsPbBr}_3$  perovskite, *ACS Omega* 5 (2020) 7468–7480.
- [39] K. Wang, C. Han, J. Li, J. Qiu, J. Sunarso, S. Liu, The mechanism of piezocatalysis: energy band theory or screening charge effect? *Angew. Chem.* 134 (2022) e202110429.
- [40] S. Tu, Y. Guo, Y. Zhang, C. Hu, T. Zhang, T. Ma, H. Huang, Piezocatalysis and piezo-photo-catalysis: catalysts classification and modification strategy, reaction mechanism, and practical application, *Adv. Funct. Mater.* 30 (2020) 2005158.
- [41] J. Shi, M.B. Starr, X. Wang, Band structure engineering at heterojunction interfaces via the piezotronic effect, *Adv. Mater.* 24 (2012) 4683–4691.
- [42] L. Ye, X. Zhu, Y. Liu, Numerical study on dual-frequency ultrasonic enhancing cavitation effect based on bubble dynamic evolution, *Ultrason. Sonochem.* 59 (2019) 104744.
- [43] S. Mukasa, S. Nomura, H. Toyota, Measurement of temperature in sonoplasma, *Jpn. J. Appl. Phys.* 43 (2004) 2833.
- [44] Z. Zhang, Y. Liang, H. Huang, X. Liu, Q. Li, L. Chen, D. Xu, Stable and highly efficient photocatalysis with lead-free double-perovskite of  $\text{Cs}_2\text{AgBiBr}_6$ , *Angew. Chem. Int. Ed.* 58 (2019) 7263–7267.
- [45] X. Fu, T. Belwal, G. Cravotto, Z. Luo, Sono-physical and sono-chemical effects of ultrasound: primary applications in extraction and freezing operations and influence on food components, *Ultrason. Sonochem.* 60 (2020) 104726.
- [46] J. Ma, S. Jing, Y. Wang, X. Liu, L.Y. Gan, C. Wang, J.Y. Dai, X. Han, X. Zhou, Piezoelectrocatalysis for  $\text{CO}_2$  reduction driven by vibration, *Adv. Energy Mater.* (2022) 2200253.
- [47] D.J. Flannigan, K.S. Suslick, Plasma formation and temperature measurement during single-bubble cavitation, *Nature* 434 (2005) 52–55.
- [48] W. Tu, Y. Zhou, Z. Zou, Photocatalytic conversion of  $\text{CO}_2$  into renewable hydrocarbon fuels: state-of-the-art accomplishment, challenges, and prospects, *Adv. Mater.* 26 (2014) 4607–4626.
- [49] X. Wang, J. He, L. Mao, X.Y. Cai, C.Z. Sun, M.S. Zhu,  $\text{CsPbBr}_3$  perovskite nanocrystals anchoring on monolayer  $\text{MoS}_2$  nanosheets for efficient photocatalytic  $\text{CO}_2$  reduction, *Chem. Eng. J.* 416 (2021) 128077.
- [50] X. Wang, J. He, X. Chen, B. Ma, M. Zhu, Metal halide perovskites for photocatalytic  $\text{CO}_2$  reduction: an overview and prospects, *Coord. Chem. Rev.* 482 (2023) 215076.
- [51] G. Liu, M. Lee, S. Kwon, G. Zeng, J. Eichhorn, A.K. Buckley, F.D. Toste, W. A. Goddard, F.M. Toma,  $\text{CO}_2$  reduction on pure Cu produces only  $\text{H}_2$  after subsurface O is depleted: theory and experiment, *Proc. Natl. Acad. Sci. USA* 118 (2021) e2012649118.